Free-Swimming Bacteria Transcriptionally Respond to Shear Flow

Ashwin Ramachandran,[1,2] Howard A. Stone,[2,*] Zemer Gitai[1,*]

[1]Department of Molecular Biology, Princeton University, Princeton NJ 08544, USA
[2]Department of Mechanical and Aerospace Engineering, Princeton University, Princeton NJ 08544, USA
*Corresponding authors: zgitai@princeton.edu (ZG) and hastone@prineton.edu (HAS)

Abstract

Surface-attached cells can sense and respond to shear flow, but planktonic (free-swimming) cells are typically assumed to be oblivious to any flow that carries them. Here we discover that planktonic bacteria can transcriptionally respond to flow, inducing expression changes that are beneficial in flow. Specifically, we use microfluidic experiments and quantitative modeling to show that in the presence of flow, planktonic *P. aeruginosa* induce shear-rate-dependent genes that promote growth in low oxygen environments. Untangling this mechanism revealed that in flow, motile *P. aeruginosa* spatially redistribute, leading to cell density changes that activate quorum sensing, which in turn enhances oxygen uptake rate. In diffusion-limited environments, including those commonly encountered by bacteria, flow-induced cell density gradients also independently generate oxygen gradients that alter gene expression. Mutants deficient in this newly-discovered flow-responsive mechanism exhibit decreased fitness in flow, suggesting that this dynamic coupling of biological and mechanical processes can be physiologically significant.

Significance statement

Bacterial pathogens commonly encounter flow in the human bloodstream and urinary tract. While previous studies have largely focused on how flow affects surface-attached bacteria, little is known about the biophysical and molecular interactions of flow with bacteria that are free-swimming and “go with the flow”. Our study focuses on the important human pathogen, *P. aeruginosa*, which is commonly associated with flow-associated infections. We discovered that under confined shear flow, planktonic *P. aeruginosa* induce expression of genes crucial for survival in low oxygen environments. We reveal that this unexpected response emerges from a flow-dependent interaction between bacterial motility mechanics, cell signaling, and oxygen-related cellular processes. Furthermore, our results suggest that this coupling of mechanical and biological responses can be physiologically beneficial.

Main text

Bacteria encounter complex and diverse mechanical environments in their lifestyle (1, 2). For example, human pathogens can cause infections in environments with flow, including the bloodstream, urinary tract, and catheters (3–5). Previous studies have focused on the effects of flow that moves past surface-attached bacteria (6–8). At the molecular level, these studies reported flow-dependent increase in intracellular cyclic-di-GMP levels (6) and increase in expression of the *fro* operon (7). While previous studies have mostly focused on surface-attached (sessile) bacteria, the effect of flow on gene expression of free-swimming (planktonic) bacteria that are being transported within the bulk of the flow has not been previously examined. Prior studies have reported that planktonic bacterial cells can spatially redistribute themselves in flow due to hydrodynamic coupling between bacterial motility and shear gradients (9, 10). Since the shear stresses experienced by individual bacterial cells are smaller than those that the bacteria experience when swimming in the absence of flow (11), hydrodynamic considerations alone would suggest that in such environments flow passively transports planktonic bacteria (12–14). As a result, the general expectation is that planktonic bacteria are carried along with the flow as inert objects, and therefore, that shear flow would not alter the gene expression of planktonic bacteria (10). However, it remains unknown whether such hydrodynamic interactions actually affect gene expression and whether bacteria can actively adapt to such environments.

Here, we directly test whether bacteria respond to being transported by flow using the bacterium *Pseudomonas aeruginosa* (PAO1), a common pathogen implicated in cystic fibrosis, bacteremia, and urinary tract infections. Surprisingly, we find that shear flow does induce significant transcriptional responses in planktonic *P. aeruginosa.* Biophysical and molecular analyses reveal that this unexpected response emerges from a flow-dependent interaction between bacterial motility mechanics, cell signaling, and oxygen-related cellular processes under confined shear flow. This previously unappreciated bacterial response is likely to be physiologically significant, as we demonstrate that it promotes metabolic adaptation that is crucial for fitness in flow environments. Our findings also suggest that the strong coupling of physical and biological processes could help to understand other aspects of how bacteria adapt and thrive in physiologically important complex environments.

Results

Transcriptomics reveals flow-sensitive gene regulation in planktonic bacteria

To determine whether flow alters the gene expression of planktonic *P. aeruginosa,* we designed a long microfluidic channel that enabled us to expose bacteria to flow for significant lengths of time and then be fixed as they exit the channel. The experiments mimic the kinds of shear flows characteristic of a wide variety of confined flow configurations. Since the shear rate varies across the channel cross-section, we characterized flow conditions in our experiments using the wall shear rate (see supplementary text). Using this microfluidic system, we performed bulk RNA-Seq analysis of planktonic bacteria that flowed for 55 min at a shear rate of 20 s^{-1}, and compared gene expression of this population with a control population of planktonic bacteria under similar conditions with no flow (**Figure 1a, Supplementary Figure 1**). We note that this shear rate is in the range that bacteria would encounter in environments like the bloodstream or urinary tract (15, 16), and that the flow field is laminar. Despite the fact that we expected that bacteria would not respond to the flow, our experiment revealed several genes that were differentially regulated between planktonic cells with and without flow (**Supplementary Table 1**). Among the most strongly flow-induced genes were several gene clusters that were previously associated with the response to low oxygen conditions (17–19), including *nar*, *arc*, and *hcn* (**Figure 1b**, **Supplementary Table 1**).

To study flow-dependent transcriptional responses in single cells and to monitor the dynamics, we engineered an *arc* transcriptional reporter PAO1 strain in which the *arc* operon promoter is fused to YFP and a constitutive *rpoD* promoter (20) is fused to mKate2 for normalization. Consistent with our RNA-Seq data, we observed that the *arc* reporter signal significantly increased with time under flow for over 1 h (**Figure 1c**). To determine the quantitative relationship between flow rate and *arc* induction, we examined the *arc* reporter under flow after 1 h at shear rates of 0 (no flow), 2, 20, and 200 s^{-1}. We observed that the induction of the *arc* reporter increased monotonically with shear rate, suggesting that planktonic bacteria under shear flow exhibit a low-oxygen transcriptional response in a flow-sensitive manner (**Figure 1d** and **Supplementary Figure 2**).

Shear flow causes swimming bacteria to redistribute and form cell density gradients

How might flow affect planktonic bacteria? To gain insight into the mechanism underlying the flow-dependent *arc* induction we examined the physical response of planktonic bacteria to shear flow in a defined rich media, EZ. Specifically, we performed phase contrast microscopy to image planktonic bacteria in shear flow in the middle of the channel (away from the surface). We observed that these bacteria distributed to create spatial gradients with more cells concentrated towards the channel walls and fewer cells concentrated towards the channel center (**Figure 2a**). We quantified this response at varying shear rates and found that the cell depletion near the channel center and the

corresponding cell enrichment near the walls both increased with shear rate (**Figure 2b** and **Supplementary Figure 3**). For example, at a shear rate of 20 s^{-1}, the cell density decreased by ~2-fold near the channel center and increased by ~2-fold near the channel walls compared to no-flow conditions.

Previous studies have suggested that hydrodynamic interactions between self-propulsion motility and shear gradients could affect the distribution of bacteria in flow (9, 10). We thus tested the effect of Type IV pilus (T4P) and flagellum-dependent motility mutants on our flow-dependent redistribution pattern. We found that flagellar mutants no longer established cell density gradients, while the behavior of pilus mutants resembled that of wild type PAO1, suggesting that flagellar motility is required for shear-induced cell redistribution (**Figure 2c** and **Supplementary Figure 4**). Our observations on cell redistribution in flow are consistent with previous studies on the effects of flow on rod-shaped bacteria with active swimming motility (21). This transverse redistribution of swimming bacteria in response to shear gradients has been modeled as a "shear-trapping" mechanism (**Figure 2d**) (21–23). In the shear-trapping model, bacteria near the channel walls encounter a transverse diffusive-like redistribution from the velocity gradient that aligns the cell body along the flow direction, and this counteracts rotational noise from swimming. This effect causes bacteria that are closer to the walls to remain more aligned with the flow and thus remain close to the wall (**Supplementary Figure 5**), while bacteria closer to the channel center (low shear rates) are more likely to swim away from the center. In this manner, flow causes bacteria to tend to migrate away from the center of the channel and get trapped near the walls over a short diffusive timescale (22, 23).

A key feature of the shear-trapping model is that it depends on the velocity gradient, whose magnitude is the shear rate, but not the shear stress. To test if the shear-trapping model is likely to explain the cell density gradients we observed, we varied the viscosity of the cell media because increased viscosity increases the shear stress without increasing shear rate for a given flow rate. We found that the bacterial cell density distribution in flow did not change significantly upon increasing viscosity (**Supplementary Figure 6**), confirming that the velocity gradient is the primary driver in setting the cell density profiles in flow.

The transcriptional flow response requires flagellar motility, quorum sensing, and oxygen sensing

The experiments above demonstrate that flow induces both transcriptional induction of *arc* and cell density changes. Furthermore, the density changes require flagellar motility (21) and *arc* is known to be regulated by the Anr oxygen sensing system (24). To

understand how each of these processes affect *arc* induction in flow, we assayed flow-dependent *arc* induction and cell density redistribution in mutants that disrupt cell density sensing (the quorum sensing master regulator, *lasR* (25, 26)), cell motility (*fliC* for flagellar motility and *pilA* for T4P (27, 28)), and oxygen sensing (*anr*) (24, 29). *pilA* had no effect on cell density or *arc* induction compared to wild-type (WT), both *anr* and *lasR* deletion cells resembled WT with respect to cell density gradients but failed to induce *arc* in flow, and *fliC* was defective in both cell density redistribution and *arc* induction (**Figure 2c**, **2e**, and **Supplementary Figure 4**). We also validated the flow response of the *anr* and *lasR* mutants by complementation (**Supplementary Figure 7**). Based on these data, we hypothesize that the cell density gradients that are established in flow due to flagellar motility subsequently induce *arc* expression through the LasR and Anr regulators.

Bacterial redistribution in flow leads to increased oxygen uptake rate via cell density sensing

The dependence of *arc* induction in flow on motility-driven cell gradient formation suggested that the cell density gradient that occurs in flow might produce an oxygen concentration gradient that activates Anr. To test this hypothesis, we obtained *in situ* measurements of oxygen concentration in the middle of the channel by measuring the fluorescence of an oxygen-sensitive dye dissolved in EZ media after 1 h of shear flow (see supplementary text). Counter to our hypothesis, we did not observe an oxygen gradient in these conditions, suggesting that there is an alternative mechanism explaining *arc* induction in flow (**Figure 3a**). For example, if flow caused bacteria to consume oxygen at a higher rate, the overall level of oxygen would decrease more quickly in flow than in the absence of flow, causing Anr to be activated by flow despite the absence of a spatial oxygen gradient. Consistent with this idea, our oxygen sensor revealed that overall oxygen levels decreased in flow faster than in the absence of flow over the course of one hour in EZ media (**Figure 3b**). We then quantified oxygen uptake rate by averaging the measured oxygen concentration across the field of view and comparing this average value measured at different locations along the channel (equivalently, in time). Under flow, the wild-type PAO1 consumed oxygen at a rate that was ~30% higher than the no-flow condition (**Figure 3c**).

Why do *P. aeruginosa* cells consume oxygen at higher rates under flow? We wondered if this increased uptake rate of oxygen in flow was related to the other transcriptional regulator we found to affect flow-dependent *arc* induction, the LasR quorum sensing master regulator. Indeed, the oxygen consumption rate of Δ*lasR* mutants was not flow dependent and resembled the oxygen consumption rate that WT exhibited under no flow conditions even when Δ*lasR* was exposed to 20 s^{-1} flow for one hour (**Figure 3c** and **Supplementary Figure 8**). Similarly, loss of flagellar motility, which eliminated the cell

density redistribution, also caused the bacteria to lose the flow dependence of oxygen consumption. Meanwhile, *anr* mutants maintained flow-dependent oxygen consumption similar to that of WT (**Figure 3c** and **Supplementary Figure 8**). These results suggest that motility-dependent changes in bacterial cell density activate quorum sensing through LasR and that LasR induction increases the oxygen consumption rate.

To determine if the LasR-mediated regulation of oxygen uptake rate depends on flow, we also quantified the oxygen uptake rate in WT and Δ*lasR* strains using spent media or increased cell concentration in the absence of flow within the microfluidic channel. We observed that only the wild-type strain showed an increase in oxygen uptake rate in both conditions, suggesting that the regulation of oxygen uptake rate via *lasR* is a flow-independent response (**Supplementary Figure 9**). This result is consistent with previous studies that have implicated quorum sensing in *P. aeruginosa* in metabolic changes that can explain the effect of cell density on oxygen consumption rate (17, 19, 30–32). At the transcriptional level, quorum sensing regulates multiple genes involved in both aerobic and anaerobic metabolism, as nearly 20% of the quorum sensing regulon is associated with oxygen-related cellular pathways including carbon compound catabolism, denitrification, amino acid metabolism, arginine biosynthesis, and energy metabolism (30, 31). Prior studies have also reported that under oxygen-limiting conditions such as those encountered in cystic fibrosis, a deficiency in quorum sensing via *lasR* induces anaerobic metabolic pathways (19, 33, 34). Together, these data suggest that shear flow of planktonic bacteria leads to an overall increase in oxygen uptake rate, and this requires the coupling of swimming motility with the ability to sense cell density changes in flow.

Diffusion-limited conditions can lead to oxygen gradients in shear flow

To better understand oxygen sensing at a quantitative level we developed a reaction-diffusion model to describe how flow affects oxygen concentration fields in the presence of cell density gradients. This model suggested that spatial oxygen gradients should emerge when oxygen diffusion is slower than the oxygen consumption rate (**Supplementary Figure 10**). To test if the absence of an oxygen gradient observed in WT PAO1 in EZ media is due to the rapid diffusion of oxygen in these conditions with cell density gradients, we decreased oxygen diffusion 10-fold by increasing the viscosity of the EZ media with added Ficoll (7) (the diffusion versus viscosity correspondence follows the Stokes-Einstein relation). To focus on changes in oxygen diffusion rather than effects on oxygen consumption rate, we performed these experiments in Δ*lasR* mutants. As predicted by the model, we found that Ficoll supplementation caused these bacteria to produce significant oxygen gradients, as measured by our oxygen sensor dye (**Figures 3d** and **3e**). Moreover, we also discovered that in these diffusion-limited conditions, *arc* induction occurred even in the absence of *lasR* (**Figure 3f**). These results suggest that

motility-dependent cell density changes in flow can sustain spatial oxygen gradients that are sufficient to alter bacterial gene expression when oxygen diffusion is limited.

We were surprised to discover that unlike in EZ media, oxygen gradients were sustained in LB media even in the absence of Ficoll (**Figures 3d** and **3e**). To quantify the effect of LB on oxygen diffusion we turned to our validated reaction-diffusion model. The measured oxygen diffusion coefficient in water at room temperature is $2x10^{-9}$ m^2/s. Using this value accurately captures our experimentally-measured oxygen gradient profile in EZ media without Ficoll, and reducing this value 10-fold accurately captured the gradients measured in EZ media with Ficoll supplementation (**Figure 3e**). However, this oxygen diffusion coefficient failed to fit our data for LB. Varying the oxygen diffusion coefficient value revealed that the model fit was best with an oxygen diffusion coefficient of $0.7x10^{-9}$ m^2/s (**Supplementary Figure 11**). The viscosity of LB and EZ media are similar, suggesting that their difference in oxygen diffusion could result from oxygen's interactions with the complex macromolecules found in LB but absent from EZ. We tested this interpretation by adding tryptone and yeast extract (complex components of LB) individually to EZ media in concentrations typically used for LB. In both cases, we observed that adding these components produced small gradients in oxygen concentration across the channel width, suggesting that macromolecular components in LB media tend to slow the diffusion of oxygen (**Supplementary Figure 11**).

Oxygen sensing promotes planktonic bacterial fitness in shear flow

Our observations that planktonic bacteria induce a transcriptional response to shear flow raise the question of whether this transcriptional response provides a fitness advantage. To assess the potential fitness benefits of flow-induced transcription we compared the growth rates of planktonic WT PAO1 and mutants defective in *arc* induction in flow. Specifically, we monitored the growth of each strain after subjecting the cells to flow at varying shear rates for over 2.5 hours (roughly two doubling times). In WT PAO1 we observed no growth rate changes as a function of flow. We next assayed growth in Δ*anr* mutants, as these cells redistribute to form cell gradients and exhibit flow-induced changes in oxygen uptake, but are defective in oxygen sensing. We observed that the Δ*anr* strain showed a significant decrease in growth rate at higher shear rates (**Figure 4a**), suggesting that there is an adaptive benefit to oxygen sensing for planktonic cells in flow. In contrast, Δ*fliC* cells, which do not redistribute and thus do not preferentially deplete oxygen in flow, and Δ*lasR* cells, which do not increase oxygen uptake and thus also do not preferentially deplete oxygen in flow, had similar growth rates across all flow rates. These data suggest that WT PAO1 utilizes the Anr oxygen sensing pathway to help it adapt to the low oxygen environment induced by flow's effects on motile planktonic cells.

Discussion

Here we present data suggesting a biophysical model for how interactions between hydrodynamics and bacterial processes like motility, metabolism, and signaling cause planktonic bacteria to alter their gene expression to provide adaptive benefits in the presence of shear flow (**Figure 4b**). First, shear flow causes bacterial cells to redistribute and become more crowded near the channel walls via shear trapping, which results from the interaction of flagellar motility and hydrodynamics of shear flow. Unexpectedly, we found that under conditions where oxygen diffusion is not limited, the changes in cell distribution caused by shear trapping leads to significant gene expression changes that influence key aspects of bacterial physiology like oxygen uptake rate. The resulting increased oxygen uptake reduces the overall oxygen concentration in the flow environment. This lower oxygen concentration is sensed by Anr, resulting in flow-induced upregulation of genes associated with microaerobic and anaerobic conditions. Independent of quorum sensing, if the cells are present in an environment where oxygen diffusion is limited, the greater oxygen consumption resulting from the higher cell density near the walls is sufficient to establish a spatial oxygen gradient, resulting in low-oxygen niches and an Anr-mediated transcriptional response. Previous studies showed that surface-attached bacteria can transcriptionally respond to flow (6–8) and swimming bacteria can hydrodynamically respond to flow (21, 22). However, our results provide the first evidence that planktonic bacteria modulate their gene expression profiles in flow. Importantly, this newfound adaptive response to flow appears to be functionally significant because mutants that cannot transcriptionally respond to flow exhibit compromised fitness in flow environments.

Our study highlights how the coupling of bacterial mechanics in shear flow and regulation of cell density-dependent metabolic processes can lead to unexpected behaviors of bacterial populations in complex environments. We note that a purely mechanics-based consideration would have predicted that planktonic bacteria should form cell density gradients in flow and be passively transported by flow and thus not have any molecular responses to flow. The finding that the bacterial motility and signaling pathways enable them to sense and respond to flow thus illustrate the complex behaviors that can emerge when living systems interact with their mechanical environments.

While the conditions we tested here used a simple channel geometry and standard culture media, our study also points to the possibility of diverse interactions between populations of planktonic cells and flow in physiologically relevant contexts. For example, most current studies assume that the diffusion of oxygen in biological systems is similar to the diffusion of oxygen in water. However, our observation that oxygen diffusion is limited in media

with complex solutes suggests that biological fluids such as blood and plasma can present constraining environments for the free diffusion of oxygen (35). This finding thus calls for a careful reevaluation of oxygen diffusion in biological systems instead of assuming a standard value across all media compositions and conditions.

While our study was primarily focused on oxygen transport and metabolism under flow, the motility-dependent cell density gradients established in flow could also lead to concentration gradients of other molecules such as nutrients, signaling molecules, proteins, and secondary metabolites. Indeed, these molecules all diffuse more slowly than molecular oxygen, so they would be predicted to form even stronger gradients (**Supplementary Figure 9**). This further points to the possibility that cells are likely to encounter a complex spatially stratified biochemical landscape under confined shear flow, which would not be seen in standard laboratory growth conditions. The effect of such a complex biochemical landscape around bacteria in shear flow on physiological fitness and adaptation over both short and long-timescales remains to be explored in detail.

Given how intricately the swimming motility of bacteria is coupled with the biophysical and molecular response under flow, it remains to be seen how other cell types respond when they are carried along by flow. To begin to address this question we tested another rod-shaped swimmer *E. coli*, and observed shear-trapping induced cell redistribution in flow similar to *P. aeruginosa* (**Supplementary Figure 12a**). However, unlike *P. aeruginosa*, *E. coli* did not exhibit flow-induced low oxygen transcriptional response under similar conditions (**Supplementary Figure 12b**), highlighting how different species respond differently to flow. Moreover, cells with distinct shapes or motility mechanisms will have different hydrodynamic interactions with shear flow that could result in different emergent behaviors. Beyond examining how additional bacterial and eukaryotic species respond to flow individually, it will prove interesting to understand how flow affects the biophysical and biochemical interactions of planktonic polymicrobial communities like those of free-floating microbiome bacteria in the lumen and mucosa of the human gastrointestinal tract (36). Thus, our findings that bacteria are not merely transported by flow but rather actively respond to this complex environment presents an important step towards understanding the interconnected ways by which the coupling of biology and mechanics can produce surprising yet physiologically-significant adaptations.

Methods

Bacterial strains and culture conditions

A list of the strains used in this study can be found in **Supplementary Table 2**, the plasmids used are described in **Supplementary Table 3**, and the primers used are described in **Supplementary Table 4**.

P. aeruginosa PAO1 was grown overnight in liquid EZ rich defined medium (37) (Teknova) or lysogeny broth (LB) Miller (Difco) in a floor shaker at room temperature of 25°C. Prior to flow experiments, overnight-grown cultures were diluted 1:200 in fresh media and grown to mid-exponential phase (OD of 0.4-0.5). For experiments involving Ficoll, cells were first grown to mid-exponential phase as described above in media without Ficoll, and when the cells reached the desired OD, the media was supplemented with 15% Ficoll prior to flow.

For cloning, PAO1 was grown on LB Miller agar (1.5% Bacto Agar) and on Vogel-Bonner minimal medium (VBMM) agar (200 mg/l $MgSO_4.7H_2O$, 10 g/l K_2HPO_4, 2 g/l citric acid, 3.5 g/l $NaNH_4HPO_4.4H2O$, and 1.5% agar) at 37°C, and on no-salt LB (NSLB) agar (5 g/l yeast extract, 10 g/l tryptone, 5% sucrose, and 1.5% agar) at 30°C. *Escherichia coli* S17 was grown in liquid LB Miller (Difco) in a floor shaker and on LB Miller agar (1.5% Bacto Agar) at 30°C or at 37°C. Antibiotics were used at the following concentrations: 200 µg/mL carbenicillin in liquid (300 µg/mL on plates) or 10 µg/mL gentamycin in liquid (30 µg/mL on plates) for *Pseudomonas*, and 100 µg/mL carbenicillin in liquid (100 µg/mL on plates) or 30 µg/mL gentamycin in liquid (30 µg/mL on plates) for *E. coli*.

Strains and plasmid construction

PAO1 deletion strains were constructed following the two-step allelic exchange protocol (38) using the plasmid pEXG2. Fragments ~500 bp directly upstream and downstream of the target gene were amplified from WT PAO1 using primer pairs P1/P2 and P3/P4 (**Supplementary Table 4**), respectively. The resulting upstream and downstream fragments were fused using overlap-extension PCR with primer pair P1/P4. The resulting fragment was cloned into the HindIII site of plasmid pEXG2. The pEXG2 plasmid was then integrated into *P. aeruginosa* PAO1 through conjugation with the donor strain *E. coli* S17. Mating was performed on LB plates, and the exconjugants were selected on VBMM plates containing 30 µg/mL gentamycin. Mutants of interest were counter-selected on NSLB plates supplemented with 15% (w/v) sucrose. Several single colonies were screened for the correct mutation using PCR and amplicon sequencing (SNPsaurus) with the primer pair P1/P4.

For constructing *arc* transcriptional reporter strains of PAO1, the fragment containing the *PaQa* promoter region within the plasmid pPaQa (20) was replaced with a fragment containing the *arc* operon promoter. First, the plasmid pPaQa was digested and linearized using restriction enzymes XhoI and BamHI to remove the *PaQa* promoter region. Thereafter, a region ~490 bp upstream of the start codon of the *arc* operon which contained the *arc* promoter was PCR amplified, and the resulting amplicon together with the digested plasmid were Gibson assembled. The resulting plasmid was electroporated into *E. coli* S17 for maintenance. Selective media containing carbenicillin was used for the plasmid maintenance. Plasmids were then purified from the S17 maintenance strain using the Qiagen miniprep kit and then introduced into PAO1 using electroporation.

For complementing the mutations in the Δ*anr* and Δ*lasR* strains, the open reading frames (ORFs) for the genes were amplified from the wild-type strain using PCR, and the ORFs were cloned into the plasmid pJN105 (39) between the EcoRI and XbaI sites via Gibson assembly. The resulting plasmid was electroporated into *E. coli* S17 and selective media containing gentamycin was used for plasmid maintenance. Purified pJN plasmids were introduced into the corresponding PAO1 mutants containing the *arc* reporter via electroporation, and colonies were selected using media containing gentamycin and carbenicillin. 0.1% arabinose was used in media to induce gene expression.

Microfluidic system design and flow conditions

Microfluidic channels were custom-fabricated using polydimethylsiloxane (PDMS) bonded to large glass slides (Ted Pella, USA). Molds for PDMS channels were 3D printed on an ABS-like WaterShed XC 11122 material (Proto Labs, USA). The channel had a rectangular cross-section with a depth and width of 450 μm and 1500 μm, respectively. The channel length followed a serpentine geometry with 34 straight sections that were each 150 mm long, corresponding to a total channel length of approximately 5 m. Flow conditions were characterized using the wall shear rate, given by:

$$\text{Shear rate} = 6\frac{\text{Flowrate}}{\text{width} \times (\text{height})^2}.$$

Our channel geometry enabled bacteria to be transported in flow within the channel for up to 1 h at a shear rate of 20 s^{-1}. A 6 mL bacterial suspension in media was loaded completely into a 10 mL syringe and the solution was injected into the channel using a syringe pump. The flow rate was adjusted according to the desired shear rates. For experiments at shear rate of 200 s^{-1}, a peristaltic pump was used in place of syringe pump to recirculate bacteria within the channel and enable long-duration exposure of bacterial cells to flow. All flow experiments were performed at room temperature.

RNA-Seq of planktonic bacteria in shear flow

For the RNA-Seq experiments, a branched channel section near the device outlet was used to inject 37% Formaldehyde at a flow rate equal to 1/8th of the main channel to fix planktonic bacteria in a 4% Formaldehyde (final concentration) media solution after they flowed for 55 min within the device and prior to exiting the channel (**Supplementary Figure 1**). This allowed us to collect a sufficient number of fixed bacterial cells required to perform transcriptomics on a population that was exposed to flow for a set duration. For the no-flow control, bacterial cells were incubated for 55 min under static flow conditions within the channel and then pipetted out and fixed for the same duration as flow-exposed cells. Three biological replicates were used for each condition.

RNA was extracted from fixed cells using the Qiagen RNeasy Mini kit with the following modifications to the protocol. Fixed cells were spun down at 6000 ×g for 5 min and resuspended in an 80 µL volume containing 30 mM Tris-HCL (pH 8.0), 2 mM EDTA, and 0.1% Triton-X 100, and 20 mg/mL lysozyme. Lysis was performed at 37°C for 20 min, followed by Proteinase K digestion at 65°C for 1 h. In addition, on-column DNase digestion was performed during RNA extraction as per the Qiagen RNeasy protocol. The extracted total RNA was then sent to SeqCenter (Pennsylvania) who generated libraries using Illumina Stranded RNA library preparation and RiboZero Plus rRNA depletion. Sequencing was performed by SeqCenter on either an Illumina NextSeq2000 platform providing up to 12 million paired end reads (2×51 bp) per sample, or NovaSeq X Plus, producing up to 12 million paired end 150bp reads per sample. After sequencing, SeqCenter conducted an intermediate RNA-analysis and provided normalized gene expression data for each sample and quantified differential gene expression. Quality control and adapter trimming were performed with Illumina's software bcl-convert, read mapping was performed with HISAT2 (40), and read quantification was performed using Subread's featureCounts (41) functionality. Thereafter, read counts were loaded into R and normalized using edgeR's Trimmed Mean of M values algorithm (42), and the values were converted to counts per million (CPM). Differential expression analysis was performed using edgeR's glmQLFTest functionality using no-flow condition as the control group and flow condition as the treatment group. Subsequently, a volcano plot for differential gene expression was generated by plotting $\log_2$(Fold-change) and *p*-value for each gene. For the volcano plot, a *p*-value of 0.01 was used as the threshold for significance. The parameters and versions of the tools used for RNA-Seq analysis are mentioned in **Supplementary Table 5**.

Cell density measurements in flow

Phase contrast microscopy was used to measure the cell distribution of planktonic bacteria in shear flow. Imaging was performed using a 10x objective on a Nikon Eclipse Ti

microscope connected to a digital CMOS camera (Hamamatsu ORCA-FLASH4.0). A short exposure time corresponding to the flowrate was used to avoid cell streaking and minimize scatter from the channel edges. The imaging region was chosen to be the middle of the channel cross-section, i.e., halfway deep, away from the walls at a location approximately 4 m from the channel inlet and the region of interest spanned the entire channel width. Between successive measurements at different flowrates, at least 10 min was provided for the cell density distribution to equilibrate. Thereafter, five images were taken at a given shear rate in 1 min intervals. The cell density distribution was obtained by averaging across these measurements. A custom MATLAB script was developed to calculate the cell density distribution from experimental images. Briefly, the raw images were denoised, background subtracted using a threshold, and binarized to identify individual bacterial cells and their corresponding centroids. Thereafter, the channel width was binned into 100 sections, and within each section the total number of cells was computed and normalized by mean number of cells across each section in the field of view. The resulting normalized value of cell counts was plotted versus the bin centers to obtain the cell density distribution.

To obtain the distribution of cell orientations in flow, higher resolution imaging was performed using a 60x/0.7 NA ELWD objective. Images were processed and analyzed in ImageJ (43). Briefly, raw images were denoised, background subtracted, and binarized using a threshold to identify individual cells. Thereafter, the images were skeletonized based on the threshold and were analyzed using the directionality plugin in ImageJ.

Transcriptional reporter assays

For the transcriptional reporter assays, the reporter strains were first subject to flow at varying shear rates and durations within the channel. The high speeds of bacteria during flow within the channel precluded direct fluorescence imaging of the cells during flow. Therefore, after subjecting the cells to a set duration in flow, the cell solution from the channel was immediately collected in a 1.5 mL Eppendorf tube and a ~10 µL volume of the solution was sandwiched between a cover glass and glass slide and imaged. Phase contrast and fluorescence (YFP, mKate2) microscopy was performed on a 100x/1.4 NA objective on a Nikon Eclipse Ti microscope connected to a Hamamatsu ORCA-FLASH4.0 camera. Fluorescence values from individual cells were quantified using ImageJ. The reporter signal is calculated as the mean fold-change of the fluorescence ratio of YFP and mKate2 obtained for flow conditions compared to no-flow conditions, averaged across at least 30 cells from three independent experiments.

In situ oxygen concentration and uptake rate measurements

Oxygen concentration fields within the microfluidic channel were measured using an oxygen-sensitive fluorescent dye, tris(2,2'-bipyridyl)dichloro-ruthenium(II) hexahydrate (RTDP). RTDP was dissolved in the respective media at a final concentration of 5 mg/ml. Imaging was performed on Nikon Eclipse Ti microscope connected to a Hamamatsu ORCA-FLASH4.0 camera using a 10x objective and using a blue wavelength excitation and a far-red wavelength emission filter set. The calibration between oxygen concentration and RTDP fluorescence quenching was obtained by titrating varying amounts of dissolved oxygen in media and using the Stern-Volmer relation: $I_0/I = 1 + K_{SV}[O_2]$, where I_0 and I are the fluorescence intensities without and with oxygen respectively, K_{SV} is the Stern-Volmer quenching constant, and $[O_2]$ is the concentration of the oxygen. All measurements including the calibration were performed within the microfluidic channel using the same illumination intensity and exposure time settings to maintain consistent fluorescence readouts. Oxygen uptake rates for each condition were calculated by measuring the average oxygen consumption over 1 h of the experiment normalized by the total number of bacterial cells.

Growth rate measurements

Growth rate measurements were performed using a peristaltic pump (Masterflex L/S, USA) connected to the microfluidic channel and flow within a closed-loop. Overnight-grown cells were back diluted 1:200 in fresh media and grown to an OD of 0.1 at room temperature in culture tubes with shaking. Then, the cells were loaded from the culture tubes into the channel using the pump to completely fill the channel and the connecting tubing. Thereafter, the flow loop was closed, and cells were subject to varying flow conditions for 2.5 h. After exposure to flow, the cell suspension from within the channel was collected and the final optical density (OD) at 600 nm was measured using a spectrophotometer. Growth rate was calculated according to the formula:

$$\text{Growth rate} = \frac{1}{2.5\ \text{h}} \ln\left(\frac{\text{final OD}}{\text{initial OD}}\right)$$

Reaction-diffusion transport model

To model the dynamics of oxygen concentration during flow of planktonic bacteria, we invoked the unsteady, one-dimensional reaction-diffusion model. Using the channel width coordinate y centered at channel middle, cell density distribution $\rho(y)$, diffusivity of oxygen D, cellular oxygen consumption rate λ, the evolution of oxygen concentration $n(y,t)$ in time *t* was modeled as:

$$\frac{\partial n}{\partial t} = D\frac{\partial^2 n}{\partial y^2} - \lambda\rho(y).$$

Refer to the **Supplementary Text** for details on model assumptions, derivations, and parameters. A custom MATLAB code was used to solve the above equation and simulate

the evolution of oxygen and other species' concentration fields in flow for a given experimentally-obtained distribution of planktonic bacteria.

Statistical analysis

Statistical analyses were performed using GraphPad Prism software version 9.

References

1. A. Persat, *et al.*, The mechanical world of bacteria. *Cell* **161**, 988–997 (2015).
2. Y. F. Dufrêne, A. Persat, Mechanomicrobiology: how bacteria sense and respond to forces. *Nat Rev Microbiol* **18**, 227–240 (2020).
3. B. W. Trautner, R. O. Darouiche, Catheter-Associated Infections: Pathogenesis Affects Prevention. *Arch Intern Med* **164**, 842–850 (2004).
4. H. Minasyan, Sepsis: Mechanisms of bacterial injury to the patient. *Scand J Trauma Resusc Emerg Med* **27**, 1–22 (2019).
5. G. C. Padron, A. M. Shuppara, J.-J. S. Palalay, A. Sharma, J. E. Sanfilippo, Bacteria in Fluid Flow. *J Bacteriol* **205** (2023).
6. C. A. Rodesney, *et al.*, Mechanosensing of shear by Pseudomonas aeruginosa leads to increased levels of the cyclic-di-GMP signal initiating biofilm development. *Proc Natl Acad Sci U S A* **114**, 5906–5911 (2017).
7. J. E. Sanfilippo, *et al.*, Microfluidic-based transcriptomics reveal force-independent bacterial rheosensing. *Nat Microbiol* **4**, 1274–1281 (2019).
8. G. C. Padron, *et al.*, Shear rate sensitizes bacterial pathogens to H 2 O 2 stress. *Proceedings of the National Academy of Sciences* **120**, 2017 (2023).
9. E. Lauga, Bacterial Hydrodynamics. *Annu Rev Fluid Mech* **48**, 105–130 (2016).
10. J. D. Wheeler, E. Secchi, R. Rusconi, R. Stocker, Not Just Going with the Flow: The Effects of Fluid Flow on Bacteria and Plankton. *Annu Rev Cell Dev Biol* **35**, 213–237 (2019).
11. R. Chawla, R. Gupta, T. P. Lele, P. P. Lele, A Skeptic's Guide to Bacterial Mechanosensing. *J Mol Biol* **432**, 523–533 (2020).
12. T. Rossy, C. D. Nadell, A. Persat, Cellular advective-diffusion drives the emergence of bacterial surface colonization patterns and heterogeneity. *Nat Commun* **10**, 1–9 (2019).
13. J. C. Conrad, R. Poling-Skutvik, Confined Flow: Consequences and Implications for Bacteria and Biofilms. *Annu. Rev. Chem. Biomol. Eng* **9**, 175–200 (2018).
14. E. Secchi, *et al.*, The effect of flow on swimming bacteria controls the initial colonization of curved surfaces. *Nat Commun* **11**, 1–12 (2020).
15. M. M. C. Velraeds, B. Van De Belt-Gritter, H. C. Van Der Mei, G. Reid, H. J. Busscher, Interference in initial adhesion of uropathogenic bacteria and yeasts to silicone rubber by a Lactobacillus acidophilus biosurfactant. *J Med Microbiol* **47**, 1081–1085 (1998).
16. R. H. Haynes, The Rheology of Blood. *Transactions of the Society of Rheology* **5**, 85–101 (1961).
17. C. Alvarez-Ortega, C. S. Harwood, Responses of Pseudomonas aeruginosa to low oxygen indicate that growth in the cystic fibrosis lung is by aerobic respiration. *Mol Microbiol* **65**, 153–165 (2007).

18. K. Schreiber, *et al.*, The anaerobic regulatory network required for Pseudomonas aeruginosa nitrate respiration. *J Bacteriol* **189**, 4310–4314 (2007).
19. G. Pessi, D. Haas, Transcriptional control of the hydrogen cyanide biosynthetic genes hcnABC by the anaerobic regulator ANR and the quorum-sensing regulators LasR and RhlR in Pseudomonas aeruginosa. *J Bacteriol* **182**, 6940–6949 (2000).
20. A. Persat, Y. F. Inclan, J. N. Engel, H. A. Stone, Z. Gitai, Type IV pili mechanochemically regulate virulence factors in Pseudomonas aeruginosa. *Proceedings of the National Academy of Sciences* **112**, 7563–7568 (2015).
21. R. Rusconi, J. S. Guasto, R. Stocker, Bacterial transport suppressed by fluid shear. *Nat Phys* **10**, 212–217 (2014).
22. L. Vennamneni, S. Nambiar, G. Subramanian, Shear-induced migration of microswimmers in pressure-driven channel flow. *J Fluid Mech* **890** (2020).
23. B. Ezhilan, D. Saintillan, Transport of a dilute active suspension in pressure-driven channel flow. *J Fluid Mech* **777**, 482–522 (2015).
24. M. Gamper, A. Zimmermann, D. Haas, Anaerobic regulation of transcription initiation in the arcDABC operon of Pseudomonas aeruginosa. *J Bacteriol* **173**, 4742–4750 (1991).
25. E. C. Pesci, J. P. Pearson, P. C. Seed, B. H. Iglewski, Regulation of las and rhl quorum sensing in Pseudomonas aeruginosa. *J Bacteriol* **179**, 3127–3132 (1997).
26. J. Lee, L. Zhang, The hierarchy quorum sensing network in Pseudomonas aeruginosa. *Protein Cell* **6**, 26–41 (2015).
27. L. L. Burrows, Pseudomonas aeruginosa Twitching Motility: Type IV Pili in Action. *Annu Rev Microbiol* **66**, 493–520 (2012).
28. M. Bouteiller, *et al.*, Pseudomonas Flagella: Generalities and Specificities. *Int J Mol Sci* **22**, 3337 (2021).
29. H. Arai, Regulation and Function of Versatile Aerobic and Anaerobic Respiratory Metabolism in Pseudomonas aeruginosa. *Front Microbiol* **2**, 1–13 (2011).
30. V. E. Wagner, D. Bushnell, L. Passador, A. I. Brooks, B. H. Iglewski, Microarray Analysis of Pseudomonas aeruginosa Quorum-Sensing Regulons: Effects of Growth Phase and Environment. *J Bacteriol* **185**, 2080–2095 (2003).
31. P. W. Davenport, J. L. Griffin, M. Welch, Quorum sensing is accompanied by global metabolic changes in the opportunistic human pathogen Pseudomonas aeruginosa. *J Bacteriol* **197**, 2072–2082 (2015).
32. J. H. Hammond, E. F. Dolben, T. J. Smith, S. Bhuju, D. A. Hogan, Links between Anr and quorum sensing in Pseudomonas aeruginosa biofilms. *J Bacteriol* **197**, 2810–2820 (2015).
33. M. Toyofuku, *et al.*, Quorum sensing regulates denitrification in Pseudomonas aeruginosa PAO1. *J Bacteriol* **189**, 4969–4972 (2007).
34. S. S. Yoon, *et al.*, Pseudomonas aeruginosa Anaerobic Respiration in Biofilms. *Dev Cell* **3**, 593–603 (2002).
35. S. C. Bryant, R. M. Navari, Effect of plasma proteins on oxygen diffusion in the pulmonary capillaries. *Microvasc Res* **7**, 120–130 (1974).
36. G. S. Crowther, *et al.*, Comparison of planktonic and biofilm-associated communities of Clostridium difficile and indigenous gut microbiota in a triple-stage chemostat gut model. *Journal of Antimicrobial Chemotherapy* **69**, 2137–2147 (2014).
37. F. C. Neidhardt, P. L. Bloch, D. F. Smith, Culture Medium for Enterobacteria. *J Bacteriol* **119**, 736–747 (1974).

38. L. R. Hmelo, *et al.*, Precision-engineering the Pseudomonas aeruginosa genome with two-step allelic exchange. *Nat Protoc* **10**, 1820–1841 (2015).
39. J. R. Newman, C. Fuqua, "Broad-host-range expression vectors that carry the L-arabinose-inducible Escherichia coli araBAD promoter and the araC regulator" (1999).
40. D. Kim, J. M. Paggi, C. Park, C. Bennett, S. L. Salzberg, Graph-based genome alignment and genotyping with HISAT2 and HISAT-genotype. *Nat Biotechnol* **37**, 907–915 (2019).
41. Y. Liao, G. K. Smyth, W. Shi, featureCounts: an efficient general purpose program for assigning sequence reads to genomic features. *Bioinformatics* **30**, 923–930 (2014).
42. M. D. Robinson, D. J. McCarthy, G. K. Smyth, <tt>edgeR</tt> : a Bioconductor package for differential expression analysis of digital gene expression data. *Bioinformatics* **26**, 139–140 (2010).
43. C. A. Schneider, W. S. Rasband, K. W. Eliceiri, NIH Image to ImageJ: 25 years of image analysis. *Nat Methods* **9**, 671–675 (2012).
44. R. Edgar, Gene Expression Omnibus: NCBI gene expression and hybridization array data repository. *Nucleic Acids Res* **30**, 207–210 (2002).
45. D. A. Stolpera, N. P. Revsbech, D. E. Canfield, Aerobic growth at nanomolar oxygen concentrations. *Proc Natl Acad Sci U S A* **107**, 18755–18760 (2010).
46. A. Zaslaver, *et al.*, A comprehensive library of fluorescent transcriptional reporters for Escherichia coli. *Nat Methods* **3**, 623–628 (2006).
47. H. M. Jones, R. P. Gunsalus, Regulation of Escherichia coli fumarate reductase (frdABCD) operon expression by respiratory electron acceptors and the fnr gene product. *J Bacteriol* **169**, 3340–3349 (1987).

Acknowledgements

We thank Joshua W. Shaevitz, members of the Gitai Lab, and members of the Shaevitz lab for helpful discussions and feedback. This work was supported by the National Science Foundation grant MCB 2033020 (to ZG and HAS).

Author contributions

All authors conceptualized and developed the methodologies of the study. AR performed experiments and data analysis. All authors contributed to data interpretation and writing the manuscript.

Competing interests

Authors declare that they have no competing interests.

Data availability

RNA-Seq data are freely available under the National Center for Biotechnology Information (NCBI) Sequence Read Archive submission number PRJNA1049796 and can be accessed at this link: https://www.ncbi.nlm.nih.gov/sra/PRJNA1049796. RNA-Seq discussed in this publication have also been deposited in NCBI's Gene Expression Omnibus (44) and are accessible through GEO Series accession number GSE271426

(https://www.ncbi.nlm.nih.gov/geo/query/acc.cgi?acc=GSE271426). All other data are included in the main text or the supplementary materials.

List of Main Figures

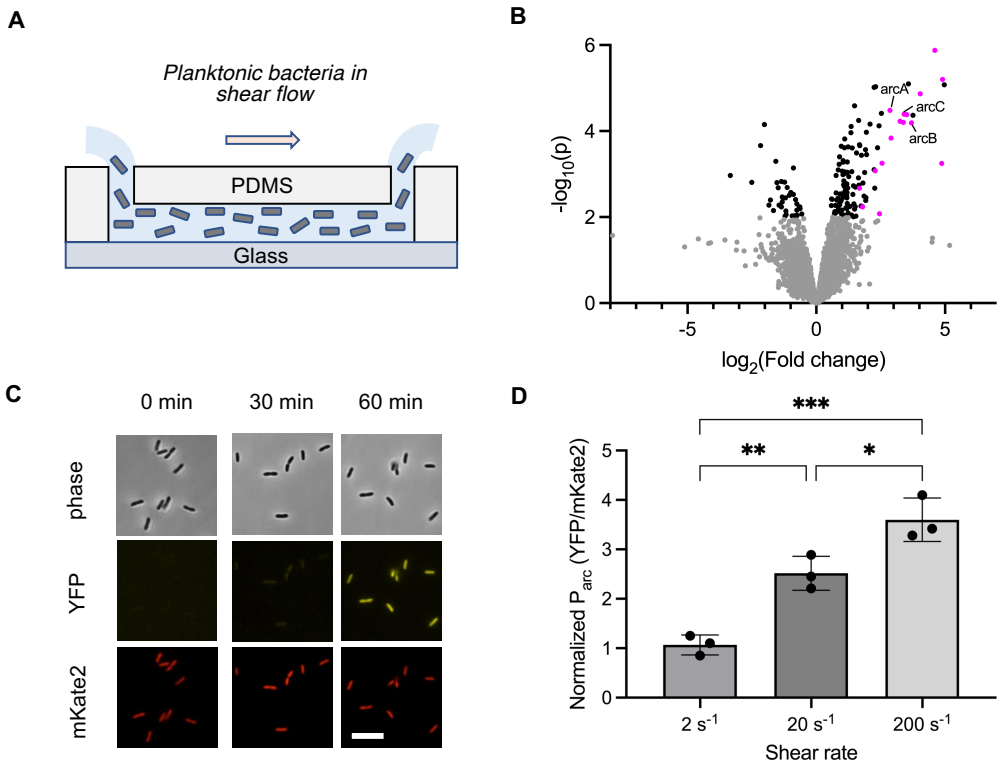

Figure 1. Flow induces transcription of low-oxygen genes in planktonic *P. aeruginosa*. (**A**) Schematic of microfluidic system used in this work to study the interaction between planktonic bacteria and shear flow. Refer to **Supplementary Figure 1** for detailed chip configuration and dimensions. (**B**) Volcano plot representing significance versus fold-change of transcripts from bulk RNA-Seq of *P. aeruginosa* that flowed in the channel for 55 min at 20 s^{-1} compared to transcripts from cells under no flow conditions within the channel for the same duration. Gene expression was evaluated using three biological replicates for each condition. A *p*-value of 0.01 is used as the threshold for significance. Symbols in magenta represent genes that are upregulated under low oxygen conditions (see **Supplementary Table 1** for a complete list of these genes and for all the genes that are upregulated by at least three-fold due to flow). Also indicated by solid lines are genes from the *arc* operon. (**C**) Representative phase contrast and fluorescence microscopy images of cells after subjecting them to shear flow of 20 s^{-1} for 0, 30, and 60 min. YFP and mKate2 represent transcriptional reporter signals from individual cells corresponding to the transcription of the *arc* operon and constitutively expressed *rpoD*, respectively. Scale bar: 8 μm. (**D**) Relative fold change of *arc* transcriptional signal for flow at 2, 20, and 200 s^{-1} compared to no-flow conditions. The transcriptional signal for each condition was obtained as the normalized ratio of YFP to mKate2 fluorescence from individual cells, averaged across at least 30 cells from three

714 independent experiments. Error bars represent the s.d. from the three replicates and each
715 flow condition is significantly different from the other (∗∗∗: $p < 0.001$, ∗∗: $p = 0.006$,
716 ∗: $p = 0.02$). Statistical significance is calculated using one-way ANOVA.

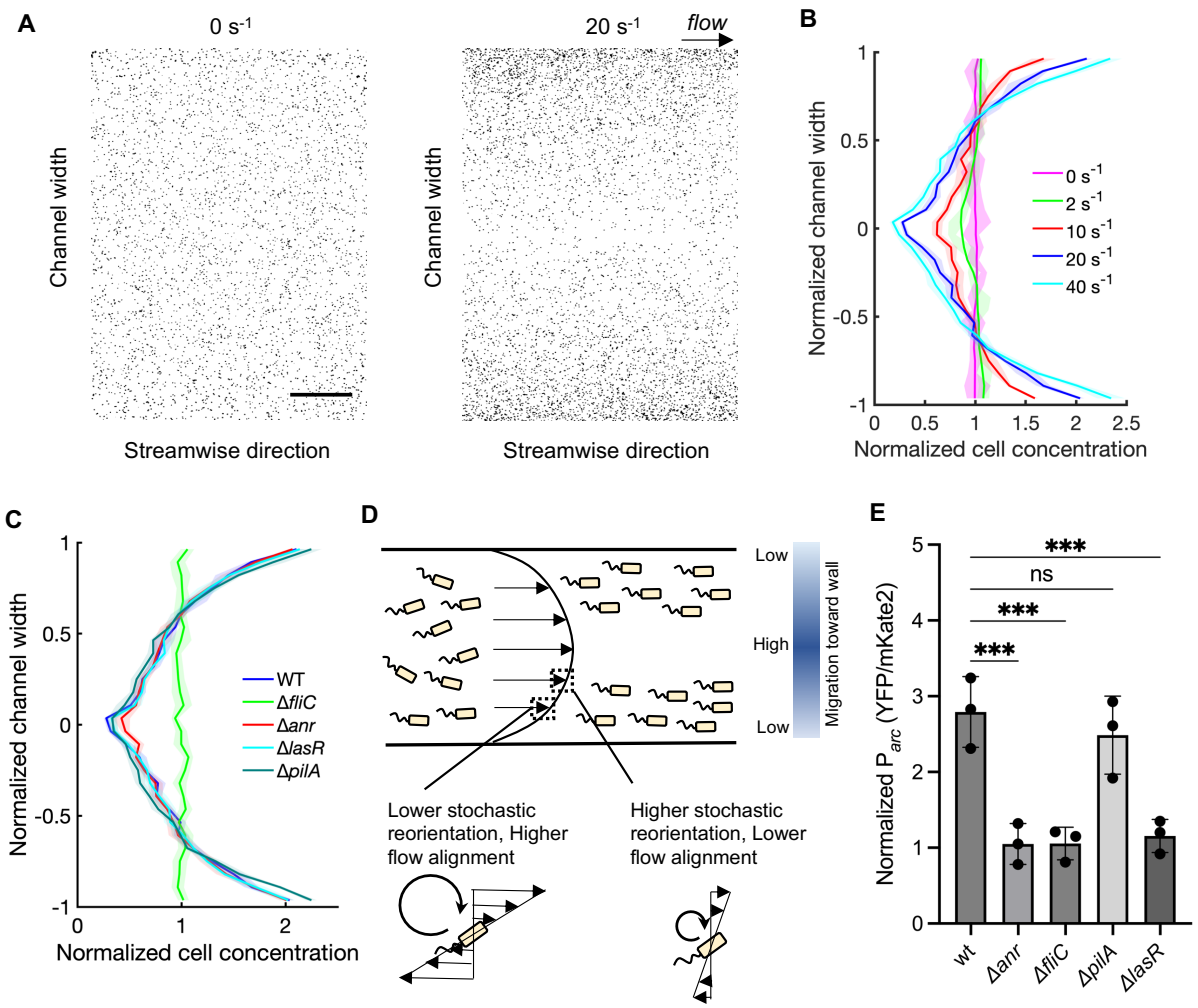

Figure 2. Flagellar motility causes planktonic bacteria to form cell density gradients in flow, and flow-mediated *arc* induction requires flagellar motility, quorum sensing, and oxygen sensing. (**A**) Instantaneous cell distribution of WT *P. aeruginosa* measured across the channel width under no-flow (0 s^{-1}) and flow at a shear rate of 20 s^{-1}. Five images were taken for each flow condition. Scale bar: 250 μm. (**B**) Cell density distribution across the channel width averaged within the field of view at shear rates of 0, 2, 10, 20, and 40 s^{-1}. The solid line and shaded regions for each condition represents the mean and standard deviation of the distribution from across five independent measurements. The channel width is normalized by the half-width of the channel. (**C**) Cell density distribution across the channel width averaged within the field of view for WT, Δ*anr*, Δ*fliC*, Δ*pilA*, and Δ*lasR* strains for flow at a shear rate of 20 s^{-1}. (**D**) Schematic of the shear-trapping model. (**E**) Normalized *arc* transcriptional reporter signal for WT, Δ*anr*, Δ*fliC*, Δ*pilA*, and Δ*lasR* strains for flow at a shear rate of 20 s^{-1}, averaged across at least 30 cells from three independent experiments. Error bars represent the standard deviation. Statistical significance is calculated using one-way ANOVA (***: $p < 0.001$, ns: not significant).

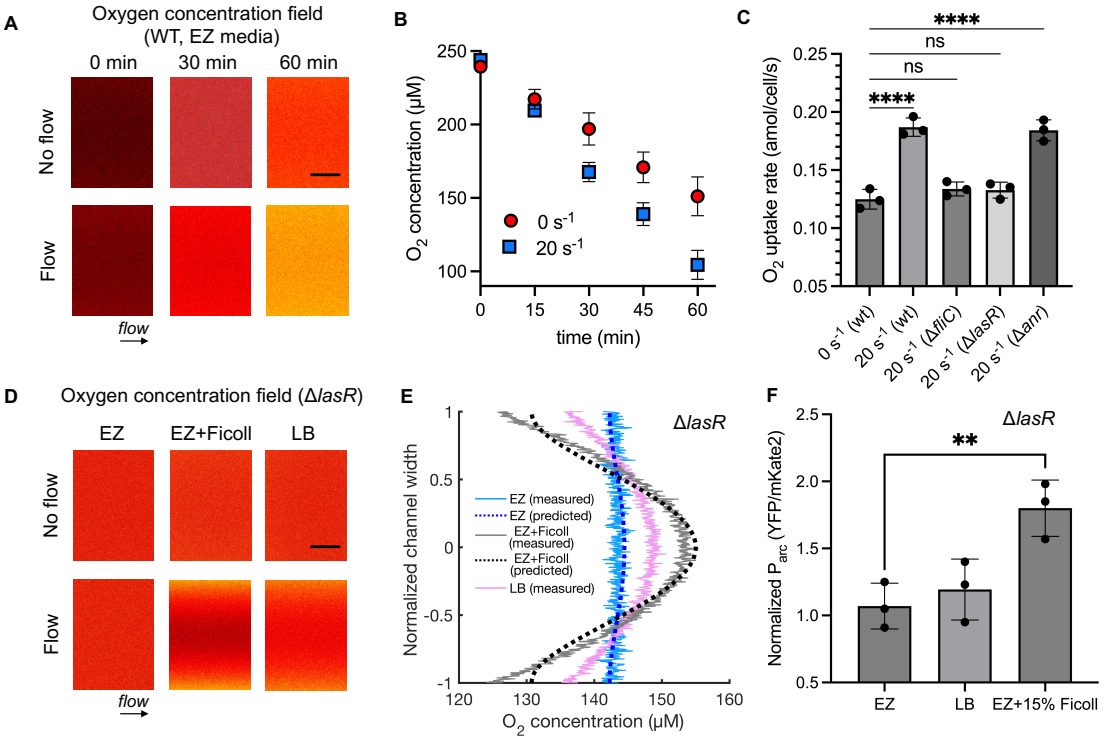

Figure 3. Quorum sensing increases oxygen uptake rate in flow, and spatial oxygen gradients form under diffusion-limited conditions. (**A**) Heatmaps depicting measured oxygen concentration fields within the channel versus time for no flow and flow at 20 s^{-1} of planktonic WT *P. aeruginosa* in EZ rich media, measured using RTDP fluorescent dye dissolved in the media (see supplementary text). RTDP fluorescence is quenched by oxygen, so an increase in fluorescence indicates reduced oxygen concentration. Scale bar: 400 μm. (**B**) Average oxygen concentration within the field of view versus time for WT *P. aeruginosa* in EZ rich media for no flow and flow at 20 s^{-1}. Plotted are the mean values from three independent experiments and the error bars represent the standard deviation. (**C**) Average oxygen consumption rate for no flow conditions of WT and for flow at a shear rate of 20 s^{-1} of planktonic WT, Δ*anr*, Δ*fliC*, and Δ*lasR* strains. Shown are the mean values and standard deviation from three independent experiments. Statistical significance is calculated using one-way ANOVA (∗∗∗∗: $p < 0.0001$, ns: not significant). (**D**) Heatmaps of measured oxygen concentration fields within the channel after 1 h of no flow and flow at 20 s^{-1} of Δ*lasR* strain in EZ, EZ + 15% Ficoll, and LB media. Scale bar: 400 μm. (**E**) Measured oxygen concentration (solid lines) averaged across the streamwise direction within the field of view versus channel width after 1 h of flow at shear rate of 20 s^{-1} of Δ*lasR* strain in EZ, EZ + 15% Ficoll, and LB media. Dashed lines represent predictions based on the reaction-diffusion model. The channel width is normalized by the half-width of the channel. (**F**) Normalized *arc* transcriptional reporter signal for Δ*lasR* strains for the same conditions as (**E**), averaged across at least 30 cells from three independent experiments. Error bars represent the standard deviation. Statistical significance is calculated using unpaired *t*-test (∗∗: $p < 0.01$).

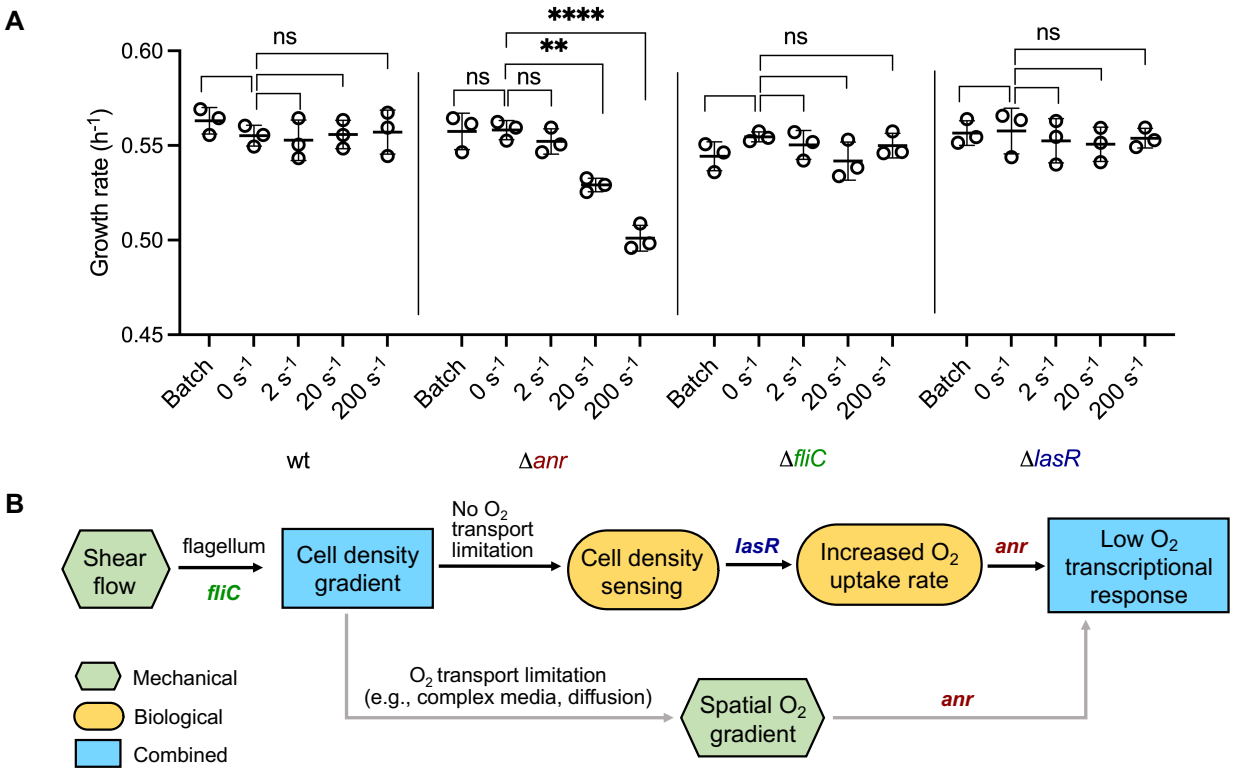

Figure 4. Oxygen sensing provides a fitness advantage to planktonic bacteria in flow. (**A**) Growth rate measurements of planktonic WT, Δ*anr*, Δ*fliC*, and Δ*lasR* strains of *P. aeruginosa* strains in batch culture and at varying shear rates of 0, 2, 20, 200 s^{-1}. Shown are individual values from three independent experiments and indicated are the mean and standard deviation. Statistical significance is calculated with respect to the no-flow condition (0 s^{-1}) using one-way ANOVA (ns: not significant, ∗∗: $p < 0.01$, ∗∗∗∗: $p < 0.0001$). (**B**) Biophysical mechanistic model for the interaction between shear flow and planktonic bacteria. Shown in green hexagons are factors that are derived purely from mechanics. A purely biological mechanism is indicated by the yellow ellipses. Blue rectangles indicate phenomena that result from combined mechanical and biological mechanisms. At each step in the mechanistic model, the corresponding genes or pathways are indicated. The black arrows represent a mechanism where there is an increase in oxygen uptake rate resulting from the coupling of flagellar motility, quorum sensing, and oxygen sensing. The gray arrows indicate a mechanism that occurs when oxygen diffusion is limited, independent of quorum sensing.

Supplementary Information for

Free-Swimming Bacteria Transcriptionally Respond to Shear Flow

Ashwin Ramachandran,[1,2] Howard A. Stone,[2,*] Zemer Gitai[1,*]

[1]Department of Molecular Biology, Princeton University, Princeton NJ 08544, USA
[2]Department of Mechanical and Aerospace Engineering, Princeton University, Princeton NJ 08544, USA
*Corresponding authors: zgitai@princeton.edu (Z.G.) and hastone@prineton.edu (H.A.S.)

The PDF file includes:

Supplementary Text
Figs. S1 to S12
Tables S1 to S5

Supplementary Text

Model for chemical species transport during shear flow of planktonic bacteria

We here present a continuum model based on reaction-diffusion transport to predict concentration profiles of chemical species around planktonic bacteria in shear flow. Our primary focus here is to model oxygen concentration profiles across the channel width, although a similar formulation can be used to model chemical interactions of bacteria with other chemical species in flow. The key idea underlying our model is that spatial gradients of bacterial cell density within the flow field resulting from shear-trapping can generate and sustain chemical species gradients via transport processes. Since the streamwise (along the flow direction) gradients in species concentration are typically much smaller than the gradients in the spanwise direction (along the channel width), we neglect local streamwise variations while describing species concentration profiles across the channel width. Therefore, we here model the species concentration distribution n as a function of the channel width coordinate y, flowrate Q, and time t that bacteria are exposed to flow.

In our model, species concentration gradients originate from motility-dependent redistribution of cells under shear flow. We assume for simplicity that the cell density distribution ρ does not change with time. This is because cells initially redistribute over a short time scale (governed by rotational diffusion) compared to the longer time scales of interest that determine species transport. Further, we assume that over the time scales of interest, cells do not divide and change in number significantly. Therefore, under these assumptions, for a given flowrate Q, the cell density distribution is only a function of the spatial location and flow conditions, i.e., $\rho(y,Q,t) \approx \rho(y,Q)$. Denoting the species diffusivity by D, the evolution of species concentration $n(y,Q,t)$ across the channel width is governed by cellular uptake and species diffusion, and is thus modeled as

$$\frac{\partial n(y,Q,t)}{\partial t} = D\frac{\partial^2 n}{\partial y^2} - \frac{\lambda n \rho(y,Q)}{n+K}, \qquad (1)$$

In Eq. (1), we have assumed Monod-type kinetics for species consumption by the cells, with Monod constant K and maximum consumption rate λ (with units mol/cell/s). In our experiments, the value of oxygen concentration in the media is in the ~100 μM concentration range and is much higher than the Monod constant for oxygen, which is typically around ~100 nM,(45) i.e., $n \gg K$. Further, we note that in our model formulation, the effect of flow conditions is implicitly incorporated in Eq. (1) via the cell density distribution term $\rho(y,Q)$, and therefore, the spatiotemporal evolution of the spanwise species concentration distribution n does not have an explicit dependence on flowrate. Therefore, we can simplify the model in Eq. (1) as

$$\frac{\partial n(y,Q,t)}{\partial t} = D\frac{\partial^2 n}{\partial y^2} - \lambda\,\rho(y,Q). \tag{2}$$

To obtain oxygen concentration profiles in **Figure 3e** and **Supplementary Figure 8a**, we numerically integrate Eq. (2) assuming experimentally derived values for uptake rate $\lambda = 0.14\ \mathrm{amol/cell/s}$ and the measured spatial cell density distribution $\rho(y,Q)$ which depends on the flowrate. We assume no-flux boundary conditions at the channel walls since diffusion of oxygen across the thick PDMS channel walls precludes efficient oxygen transport over our time scales of interest. We further assume an initial condition n_0 for oxygen concentration equal to 250 μM and assume an average cell density concentration ρ_0 of 2x10^8 cells/ml based on our experimental conditions.

Further, to predict species concentration profiles in a more general way (**Supplementary Figure 7**), we non-dimensionalize Eq. (2) by normalizing species concentration n by its initial value n_0, cell density ρ by the average value ρ_0, spatial coordinate y by channel half-width w, and time t by the diffusive time scale w^2/D, to obtain

$$\frac{\partial N}{\partial T} = \frac{\partial^2 N}{\partial Y^2} - \mathrm{Da}\,\mathrm{P}. \tag{3}$$

Here, $N = n/n_0$, $Y = y/w$, $T = tD/w^2$, $\mathrm{P} = \rho/\rho_0$, $Da = \frac{\lambda\rho_0}{n_0}\frac{w^2}{D}$ is the Damköhler number of the second kind, and the non-dimensional cell density P depends on flow conditions. Da is a non-dimensional number that represents the uptake rate versus the rate of diffusion, or equivalently, the ratio of the diffusion timescale across the channel width versus the timescale of cellular uptake. Therefore, for a given uptake/consumption rate, a lower species diffusivity corresponds to a higher Da. Lastly, to obtain steady-state species concentration profiles (which is typically obtained after several diffusion time scales) in **Supplementary Figure 7**, we set the left-hand side in Eq. (3) to zero.

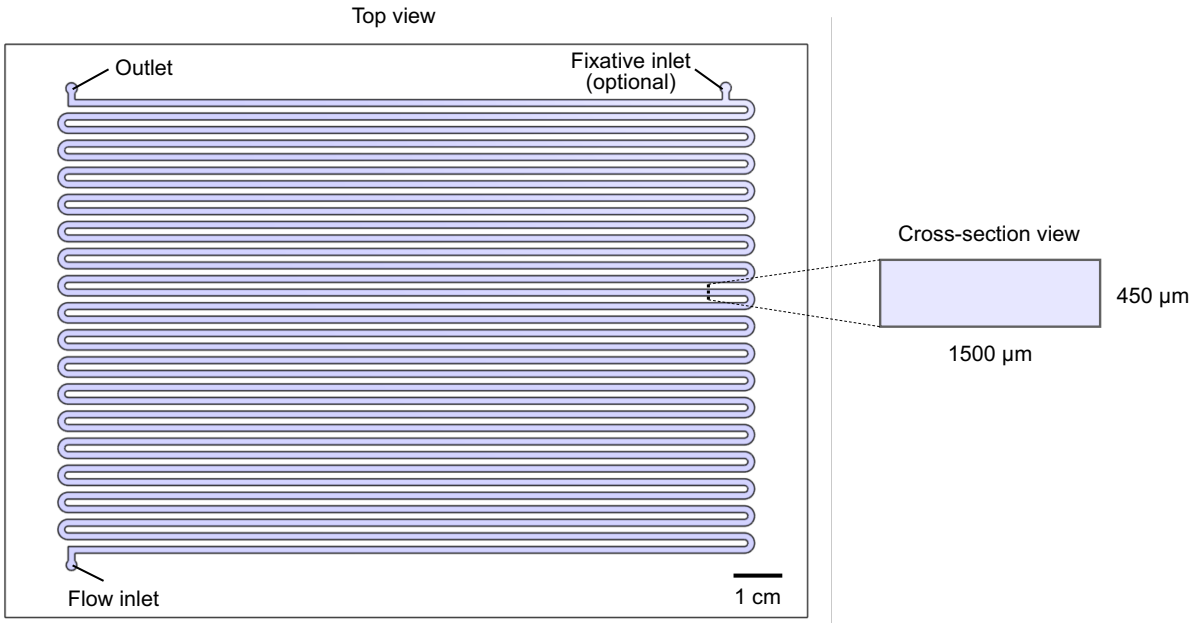

Supplementary figure 1. Detailed schematic of the microfluidic chip used in this study. Bacterial solution was flowed into the channel from the inlet and a channel length of ~ 5 m enabled flow of cells at 20 s^{-1} for 1 h. A branched channel was optionally used in RNA-Seq experiments to flow in 37% Formaldehyde at 1/8th of the flowrate in the main channel to fix bacteria prior to exiting the channel at the outlet.

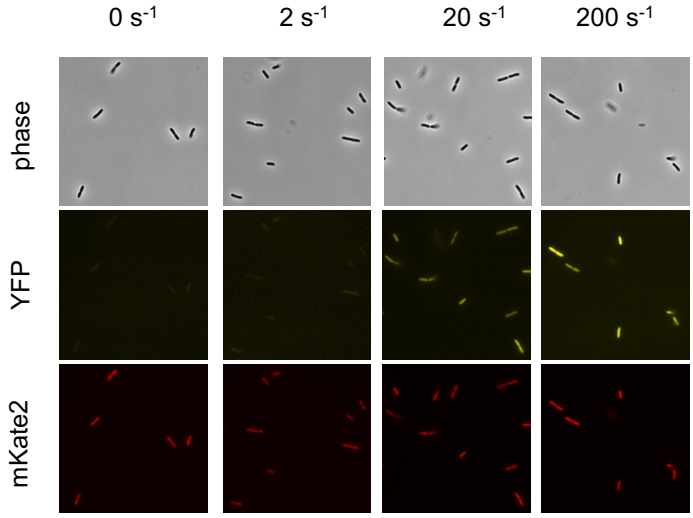

Supplementary figure 2. Phase contrast and fluorescence microscopy images of cells after subjecting them to flow at varying shear rates of 0, 2, 20, and 200 s^{-1} for 60 min. YFP and mKate2 represent transcriptional reporter signals from individual cells corresponding to the transcription of the *arc* operon and constitutively expressed *rpoD*, respectively.

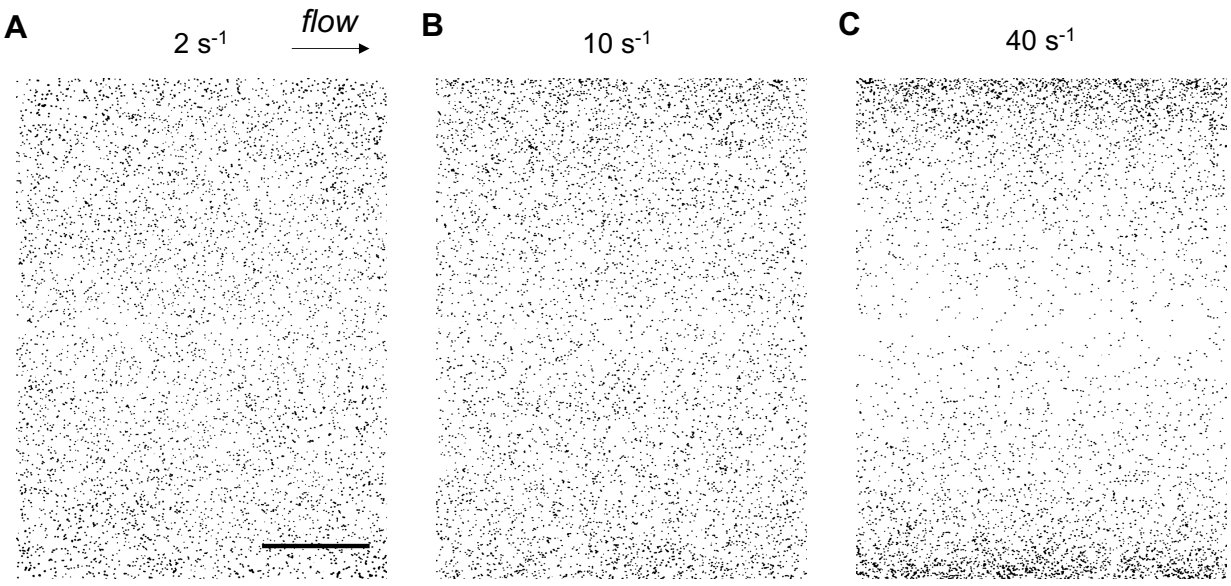

Supplementary figure 3. Cell distribution of WT *P. aeruginosa* measured across the channel width for shear rates of (**A**) 2 s^{-1}, (**B**) 10 s^{-1}, and (**C**) 40 s^{-1}. Scale bar: 300 μm.

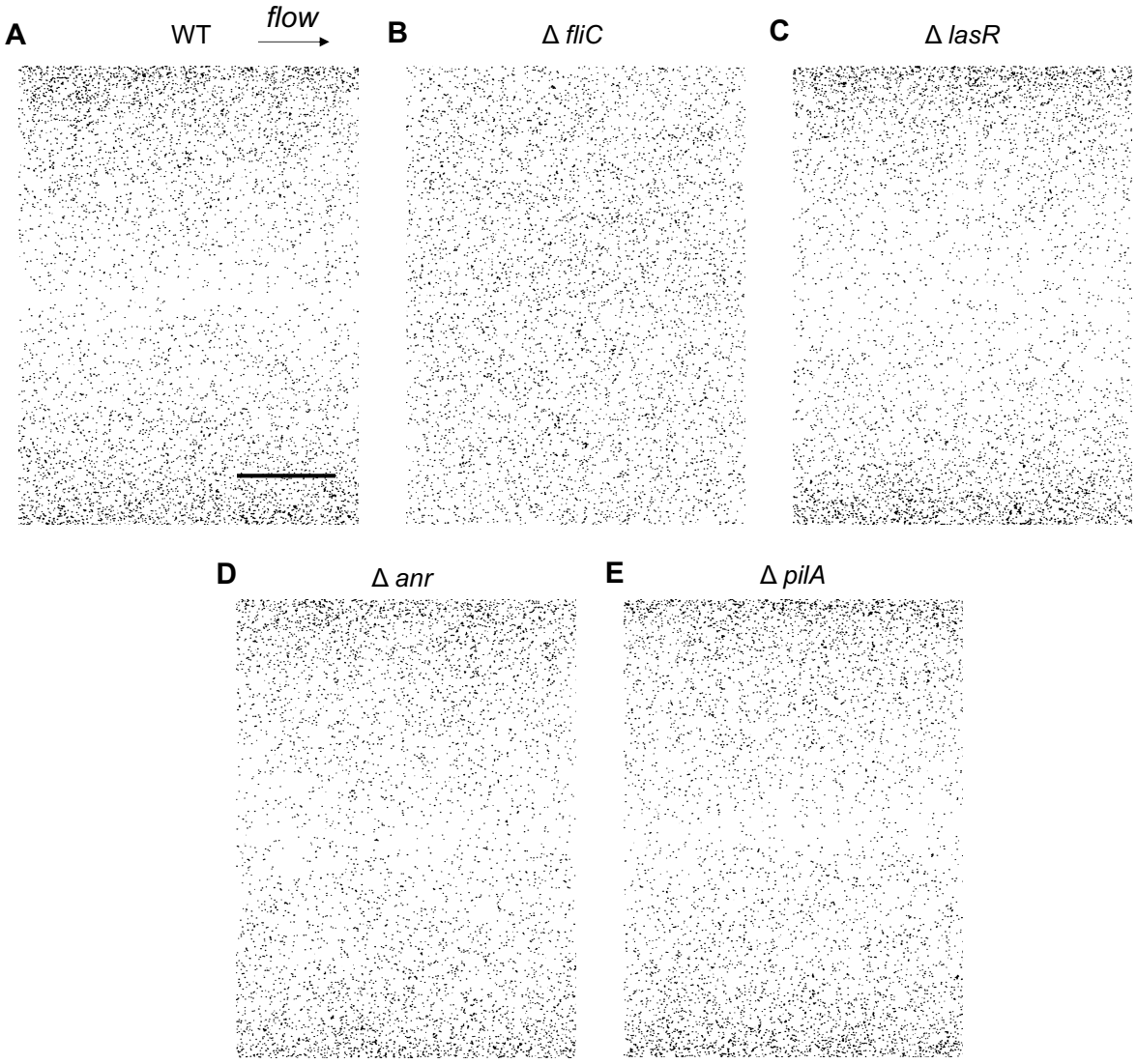

Supplementary figure 4. Cell distribution measured across the channel width at a shear rate of 20 s^{-1} for the following *P. aeruginosa* strains in EZ media: (**A**) WT (same as Fig. 2A), (**B**) Δ*fliC*, (**C**) Δ*lasR*, (**D**) Δ*anr*, and (**E**) Δ*pilA*. Scale bar: 300 μm.

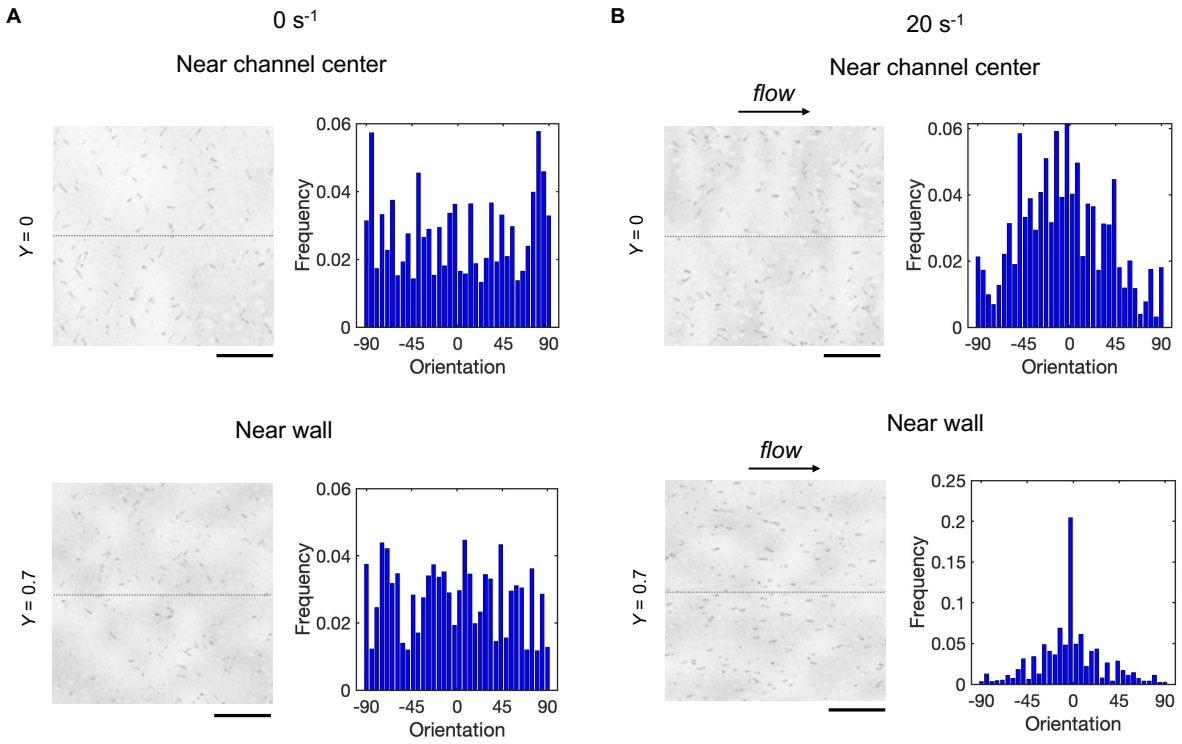

Supplementary figure 5. Instantaneous images of planktonic, wild-type *P. aeruginosa* in the microfluidic channel under (**A**) no flow (0 s^{-1}) and (**B**) flow at 20 s^{-1}, taken at locations near the channel center ($Y = 0$) and near the channel wall ($Y = 0.7$). For each flow condition and location, also shown is the corresponding distribution of bacterial cell orientation (in degrees) relative to the flow direction, averaged across three independent measurements. Scale bar: 25 μm.

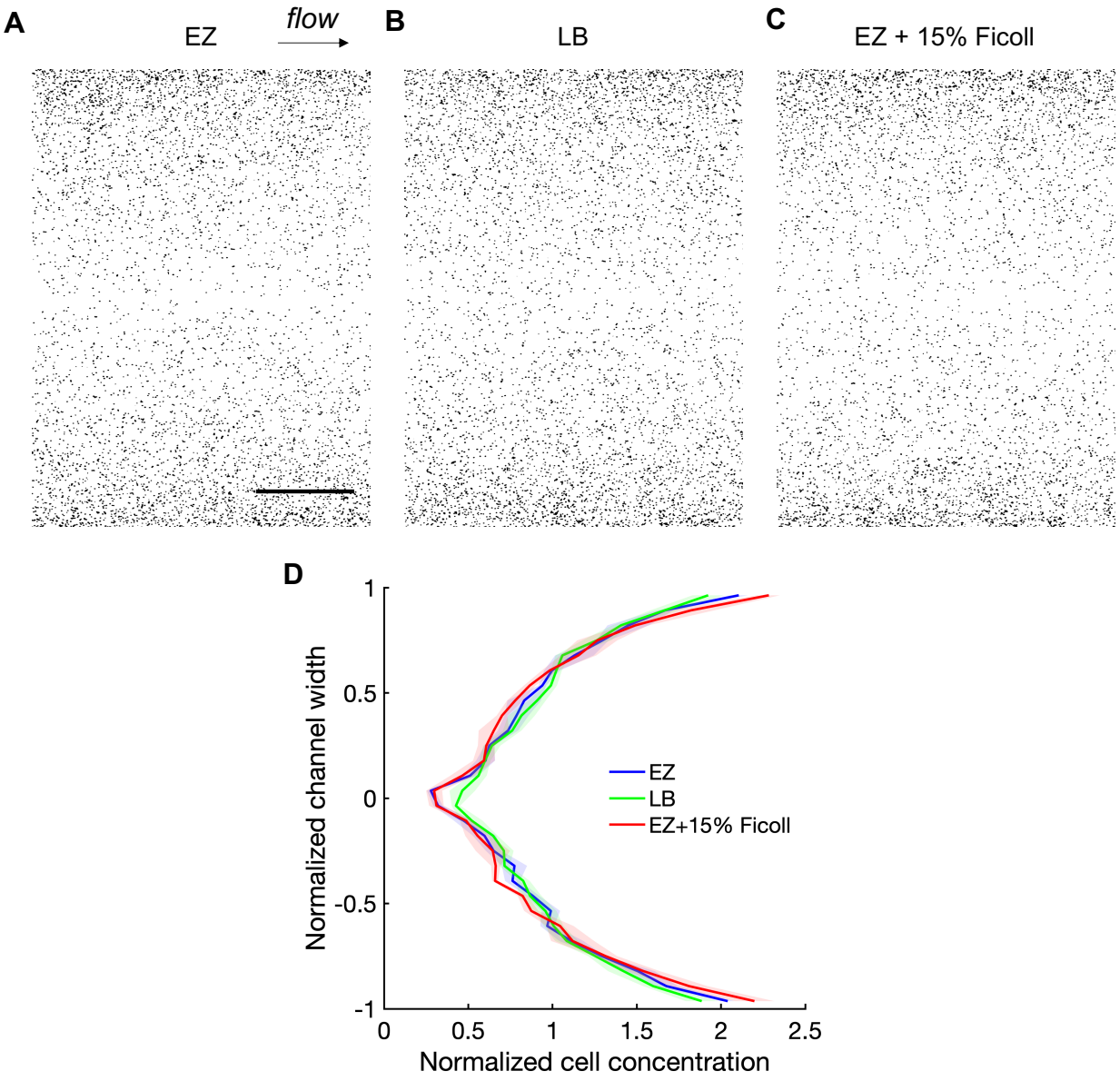

Supplementary figure 6. Cell distribution of WT *P. aeruginosa* measured across the channel width at a shear rate of 20 s^{-1} using (**A**) EZ rich media (same as Fig. 2A), (**B**) LB media, and (**C**) EZ rich media supplemented with 15% Ficoll. (**D**) Cell density distribution across the channel width averaged within the field of view for (**A**), (**B**), and (**C**). Scale bar: 300 µm.

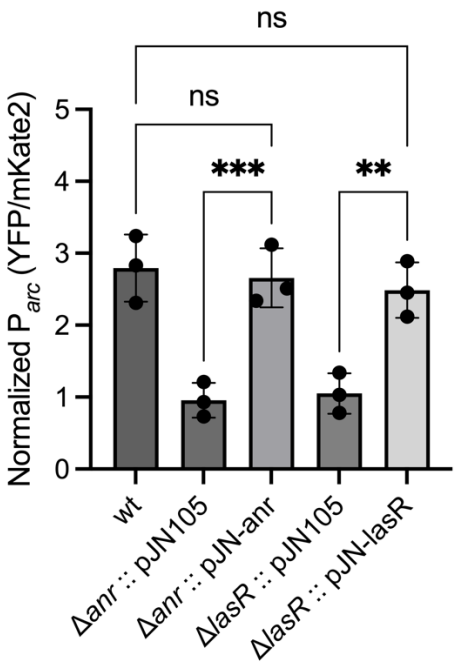

Supplementary figure 7. Relative fold change of *arc* transcriptional reporter signal for flow at shear rate of 20 s^{-1} compared to no-flow conditions for Δ*anr* and Δ*lasR* strains with and without complementation using the pJN105 plasmid backbone. Data shown are reporter signals averaged across at least 30 cells from three independent experiments. Data for WT PAO1 is the same as Figure 2E. Δ*anr* and Δ*lasR* strains carrying the empty pJN105 backbone exhibited similar behavior to the Δ*anr* and Δ*lasR* mutants in Figure 2E. Error bars represent the standard deviation. Statistical significance is calculated using one-way ANOVA (✱✱✱: $p < 0.001$, ✱✱: $p < 0.01$, ns: not significant).

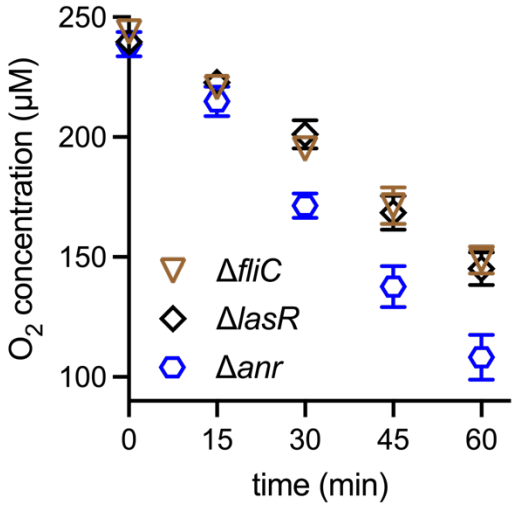

Supplementary figure 8. Average oxygen concentration within the field of view versus time for flow of Δ*fliC*, Δ*lasR*, and Δ*anr* strains of *P. aeruginosa* at a shear rate of 20 s^{-1}. Plotted are the mean values from three independent experiments and the error bars represent the standard deviation.

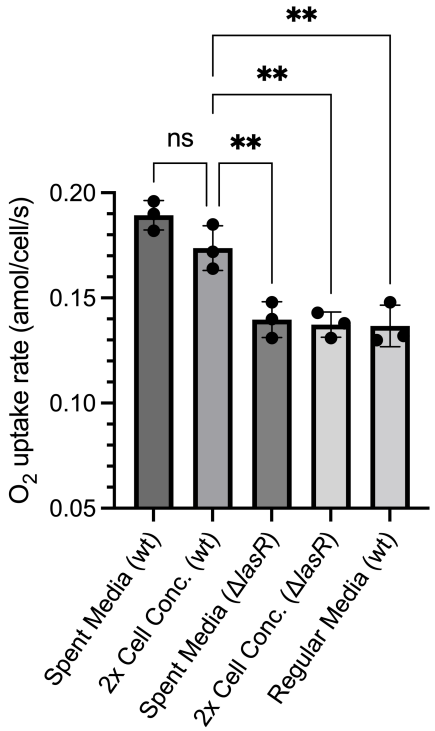

Supplementary figure 9. Average oxygen consumption rate of WT and Δ*lasR* strains obtained by reconstituting cells in spent media from overnight culture or by reconstituting cells at twice the initial cell concentration within the same media. Data presented here are under no-flow conditions for cells within the microfluidic channel. Error bars represent the standard deviation. Statistical significance is calculated using one-way ANOVA (✱✱: $p < 0.01$, ns: not significant).

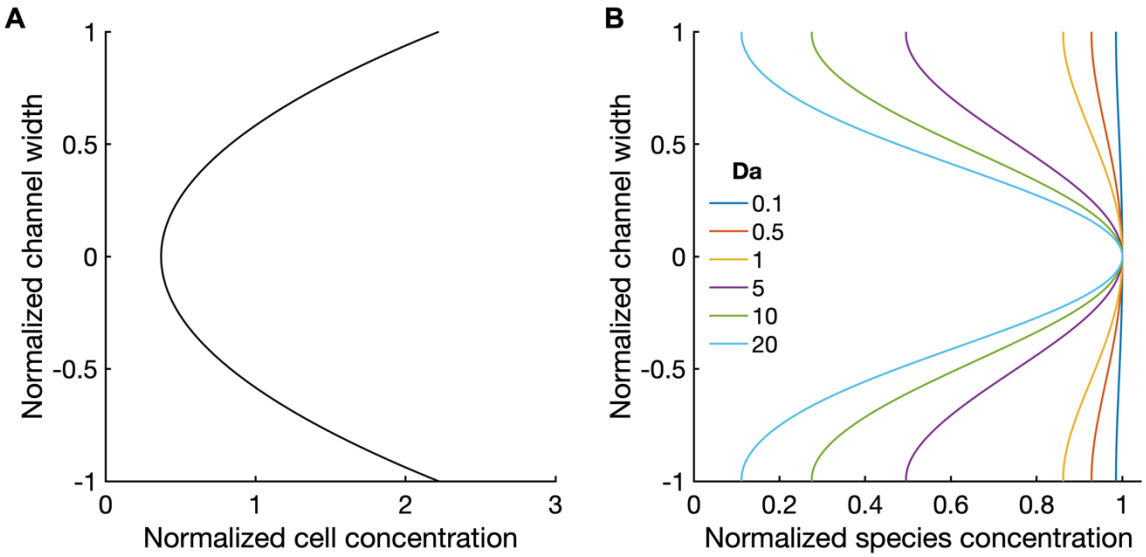

Supplementary figure 10. Concentration fields obtained from the reaction-diffusion model. (**A**) Approximate parabolic distribution for cell density distribution across the channel width used in the model, based on experimental observations for flow of WT *P. aeruginosa* at 20 s^{-1}. (**B**) Predicted steady-state concentration fields of species for varying Damköhler number (of the second kind), Da. Da is a non-dimensional number that represents the ratio of cellular uptake/consumption rate relative to the species diffusion rate. For a given uptake rate, a decrease in species diffusivity corresponds to a proportional increase in Da.

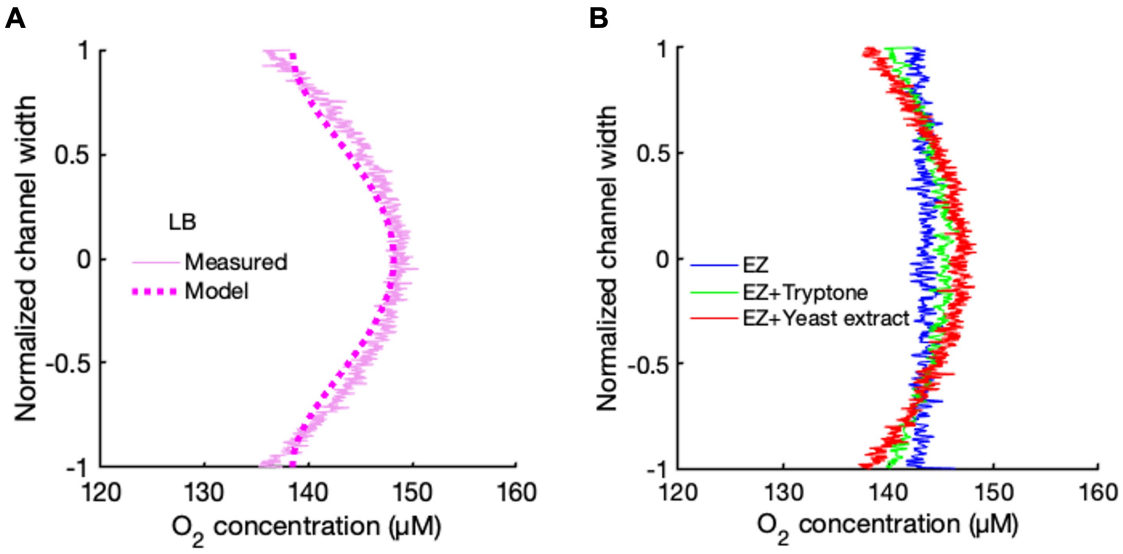

Supplementary figure 11. (**A**) Measured oxygen concentration (solid lines) averaged across the streamwise direction within the field of view versus channel width after 1 h of flow at shear rate of 20 s^{-1} of Δ*lasR* strain in LB media. Dashed lines represent the best fit using the reaction-diffusion model with an effective oxygen diffusivity of $0.7x10^{-9}$ m^2/s. (**B**) Measured oxygen concentration profiles for similar conditions as (**A**) but using EZ media supplemented with tryptone and yeast extract in concentrations typically used for LB.

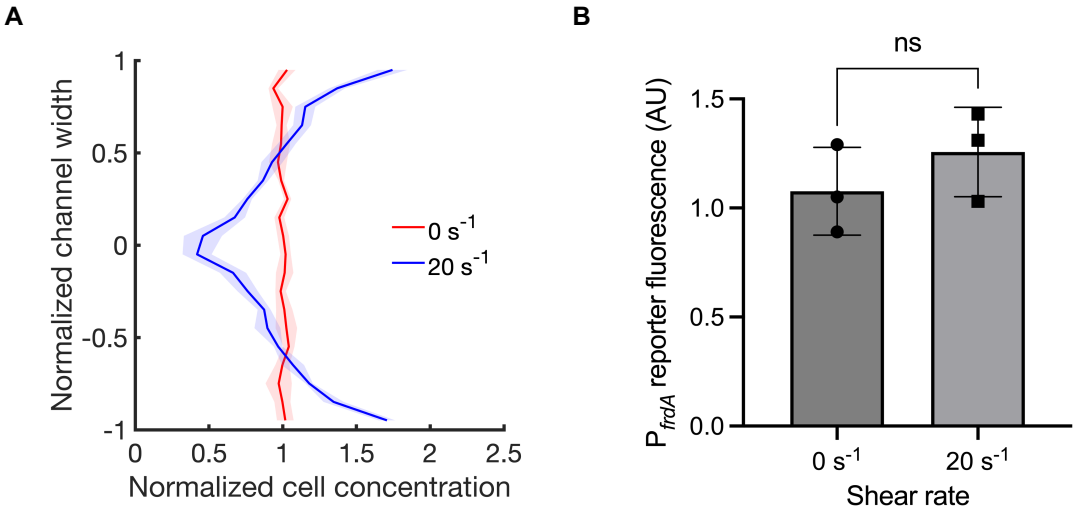

Supplementary figure 12. (**A**) Cell density distribution of *E. coli* strain MG1655 measured across the channel width for shear rates of 0 and 20 s^{-1} in EZ media. (**B**) Low-oxygen induced *frdA* transcriptional reporter signal (46, 47) for *E. coli* under the same conditions as (**A**). Error bars represent the standard deviation. Statistical significance is calculated using unpaired *t*-test (ns: not significant).

Supplementary table 1. Genes in planktonic PAO1 significantly upregulated by at least 3-fold in 20 s^{-1} flow compared to no flow based on RNA-Seq data. Highlighted genes correspond to marked symbols in **Figure 1b** which indicate genes that are typically associated with response to low-oxygen conditions.

Gene	Description	log_2(fold change)
PA1137	oxidoreductase	4.97
narI	respiratory nitrate reductase subunit gamma	4.91
narJ	respiratory nitrate reductase subunit delta	4.87
PA1746	hypothetical protein	4.61
ccpR	cytochrome C551 peroxidase	4.04
PA3871	PpiC-type peptidyl-prolyl cis-trans isomerase	3.75
arcB	ornithine carbamoyltransferase	3.70
PA0141	hypothetical protein	3.58
narH	respiratory nitrate reductase subunit beta	3.51
arcC	carbamate kinase	3.41
ccoO2	cbb3-type cytochrome C oxidase subunit II	3.38
narG	respiratory nitrate reductase subunit alpha	3.26
moaA1	molybdenum cofactor biosynthesis protein A	2.90
arcA	arginine deiminase	2.87
hcnC	hydrogen cyanide synthase subunit HcnC	2.55
PA1668	hypothetical protein	2.53
ccoN2	cbb3-type cytochrome C oxidase subunit I	2.45
PA1658	hypothetical protein	2.44
PA1666	hypothetical protein	2.38
PA1657	hypothetical protein	2.30
hcnB	hydrogen cyanide synthase subunit HcnB	2.29
PA0087	hypothetical protein	2.27
PA1662	ClpA/B-type protease	2.25
PA1660	hypothetical protein	2.24
PA1669	hypothetical protein	2.09
PA1663	transcriptional regulator	1.95
PA1667	hypothetical protein	1.95
PA1659	hypothetical protein	1.93
PA1665	hypothetical protein	1.92
PA0083	hypothetical protein	1.91
PA0088	hypothetical protein	1.88
PA5266	hypothetical protein	1.85
PA0086	hypothetical protein	1.81
nirS	nitrite reductase	1.80
PA3519	hypothetical protein	1.80
PA0084	hypothetical protein	1.75
PA3518	hypothetical protein	1.73
vgrG1	type VI secretion system protein VgrG	1.69
nosR	regulatory protein NosR	1.68
PA1845	hypothetical protein	1.68
clpV1	secretion protein ClpV1	1.66
oprG	outer membrane protein OprG	1.65
PA0089	hypothetical protein	1.64

Supplementary table 2. List of strains used in this study.

Strain	Description	Reference
E. coli		
ZG54	Wild-type S17 used for cloning and conjugation	Lab stock
ZG1845	S17 donor strain for Δ*anr* knockout in PAO1	This study
ZG1846	S17 donor strain for Δ*lasR* knockout in PAO1	This study
ZG1847	S17 maintenance strain for pArc	This study
109-AZ02_B5	MG1655 strain with GFP fused to *frdA* promoter	Ref. 41
ZG40	DH5α strain with the plasmid pJN105	Ref. 39
ZG1848	S17 maintenance strain for pJN-anr	This study
ZG1849	S17 maintenance strain for pJN-lasR	This study
P. aeruginosa		
ZG500	Wild-type PAO1 from Manoil transposon mutant library	Lab stock
ZG1850	PAO1 Δ*anr*, in frame deletion of *anr*	This study
ZG1851	PAO1 Δ*lasR*, in frame deletion of *lasR*	This study
ZG1593	PAO1 Δ*fliC*, in frame deletion of *fliC*	Lab stock
ZG525	PAO1 Δ*pilA*, in frame deletion of *pilA*	Lab stock
ZG1852	PAO1 Δ*anr*, with pArc plasmid	This study
ZG1853	PAO1 Δ*lasR*, with pArc plasmid	This study
ZG1854	PAO1 Δ*fliC*, with pArc plasmid	This study
ZG1855	PAO1 Δ*pilA*, with pArc plasmid	This study
ZG1856	PAO1 Δ*anr*, with pArc plasmid and pJN-anr for complementation	This study
ZG1857	PAO1 Δ*lasR*, with pArc plasmid and pJN-lasR for complementation	This study

Supplementary table 3. List of plasmids used in this study.

Plasmid	Description	Reference
pEXG2	Vector for generating deletion mutants	Ref. 38
pEXG2-DlasR	Δ*lasR* knockout construct	This study
pEXG2-Danr	Δ*anr* knockout construct	This study
ZG1190-pPaQa	pUCP18 backbone with PPaQa::YFP, PrpoD::mKate2	Ref. 20
pArc	pUCP18 backbone with Parc::YFP, PrpoD::mKate2	This study
pJN105	Vector for complementing expression using *araC*-P_{BAD} cassette	Ref. 39
pJN-anr	pJN105 with *anr* gene to complement *anr* deletion	This study
pJN-lasR	pJN105 with *lasR* gene to complement *lasR* deletion	This study

Supplementary table 4. List of primers used in this study.

Primer	Sequence	Reference
DlasR_P1	GATACAAAGCTTGTGAACCCGGGGACCAGGTGTG	This study
DlasR_P2	GGCAAGATCAGAGAGTAATAAGACCTCAACCAAGGCCATAGCGCTACG	This study
DlasR_P3	CGTAGCGCTATGGCCTTGGTTGAGGTCTTATTACTCTCTGATCTTGCC	This study
DlasR_P4	GATACAAAGCTTCGATCATCTTCACTTCCTCC	This study
Danr_P1	GATACAAAGCTTCATGTACTTCGAGGAAGGCC	This study
Danr_P2	CAATGGCCGAAACCATCCAGCTGGAAGGCTGAAGC	This study
Danr_P3	GCTTCAGCCTTCCAGCTGGATGGTTTCGGCCATTG	This study
Danr_P4	GATACAAAGCTTCCTGGGAAAGCTGTACATGC	This study
Parc_F	acaatgaacccccgcTCGAGCAAATGAAGAGCCCGGCG	This study
Parc_R	ccttattttctgcaccgggatcCCTATAGGAATTGAGAGTGAAGACATTAGG	This study
Anr_F	gttttttgggctagcgaattcatggccgaaaccatcaaggtg	This study
Anr_R	gcggtggcggccgctctagatcagccttccagctggc	This study
LasR_F	gttttttgggctagcgaattcatggccttggttgacggt	This study
LasR_R	gcggtggcggccgctctagatcagagagtaataagacccaaattaacggc	This study

Supplementary table 5. List of tools used for RNA-Seq analysis.

Tool	Version	Parameters
bcl-convert	4.2.4	default parameters
hisat2	2.2.1	default parameters + '--very-sensitive'
subread	2.0.6	featureCounts; default parameters + '-Q 20'
featureCounts	2.0.1	default parameters + '-Q 20'
R	4.0.2	default parameters
edgeR	1.14.5	default parameters